Journal of
Synchrotron
Radiation

ISSN 0909-0495

Received 2 August 2007
Accepted 5 December 2007

Fatigue life prediction for high-heat-load components made of GlidCop by elastic-plastic analysis

Sunao Takahashi,[a]* Mutsumi Sano,[a] Tetsuro Mochizuki,[a] Atsuo Watanabe[a] and Hideo Kitamura[b,a]

[a]JASRI, SPring-8, 1-1-1 Kouto, Sayo-cho, Sayo-gun, Hyogo 679-5198, Japan, and [b]RIKEN SPring-8 Center, 1-1-1 Kouto, Sayo-cho, Sayo-gun, Hyogo 679-5148, Japan. E-mail: takahasi@spring8.or.jp

A procedure to predict the fatigue fracture life of high-heat-load components made of GlidCop has been successfully established. This method is based upon the Manson–Coffin equation with a cumulative linear damage law. This prediction was achieved by consolidating the results of experiments and analyses, and considered the effects of environment and creep. A low-cycle-fatigue test for GlidCop was conducted so that environment-dependent $\Delta\varepsilon_t$–N_f diagrams for any temperature could be prepared. A special test piece was designed to concentrate the strain in a central area locally, resulting in the low-cycle-fatigue fracture. The experiments were carried out by repeatedly irradiating a test piece with an electron beam. The results of the experiment confirmed that the observed fatigue life was within a factor of two when compared with the predicted fatigue life, yet located on the safer side.

© 2008 International Union of Crystallography
Printed in Singapore – all rights reserved

Keywords: front ends; high heat load; elastic-plastic analysis; GlidCop; thermal limitation; fatigue life; creep.

1. Introduction

GlidCop, a copper dispersion strengthened with aluminium oxide, has been widely used the world over in high-heat-load components owing to its high strength especially at higher temperatures. In SPring-8 front ends, this material has also been applied to masks, absorbers (Mochizuki *et al.*, 2003) and *XY* slit assemblies (Oura *et al.*, 1998), all of which are typically subjected to a maximum power density of around 1 kW mm^{-2} at normal incidence from a standard in-vacuum undulator with a periodic length of 32 mm. While these components have been operating satisfactorily for about ten years now, the advancement of insertion devices has resulted in a progressive increase in the heat load. Recently, a plan to replace the standard undulator with a short-period undulator was proposed so that the energy range covered by the fundamental wavelength could be extended based on user demand. In this case, in order to restore the magnetic field, it would be necessary to narrow the magnetic gap and/or introduce a cryogenic permanent-magnet undulator design (Hara *et al.*, 2004). This, in turn, would result in a drastic increase in the heat load. For example, if a short-period undulator with a periodic length of 24 mm were used in a 6 mm gap, the total power would increase to around 16 kW with a peak power density of 1.6 kW mm^{-2} at the absorber position. Moreover, if the cryogenic scheme were adopted, these values could increase up to 37 kW and 2.4 kW mm^{-2}, respectively. In order to deal with this situation, we must reconsider the design condition for high-heat-load components, because the design criterion for the thermal stress is believed to be too conservative. A similar trial by collaborative research between the Advanced Photon Source and the European Synchrotron Radiation Facility is currently underway (Ravindranath *et al.*, 2006).

At present, our design is restricted to the elastic deformation region. In other words, the allowable stress is set to less than the yielding point. This corresponds to, roughly speaking, an allowable effective power density of less than approximately 15 W mm^{-2}. However, a local yielding phenomenon would rather release the stress and not cause instant fracture. Based on this concept, we decided to extend our design to the plastic deformation region.

Therefore, the final objective of this study is to present the acceptable power for each currently existing high-heat-load component quantitatively, including low-cycle-fatigue evaluation. In this paper we present a concrete procedure of fatigue life prediction by consolidating the results of experiments and analyses.

2. Fatigue property of GlidCop

We investigated the low-cycle-fatigue property of GlidCop in a vacuum, in addition to the basic thermal and mechanical properties in air obtained in previous tests (Takahashi *et al.*,

Table 1
Environment-dependent material properties of A, B, α and β in equation (1).

A and B are independently expressed as a function of temperature (T).

		Manson–Coffin		Basquin	
Environment	T (K)	A	$-\alpha$	B	$-\beta$
Atmosphere	373	60.8	−0.6	1.15	−0.086
	473	51.9	−0.6	1.01	−0.086
	673	30.9	−0.6	0.71	−0.086
	Any	$-0.1T + 71.31$	−0.6	$-0.0015T + 1.295$	−0.086
Vacuum	473	31.2	−0.48	1.1	−0.086
	573	24.6	−0.48	0.95	−0.086
	Any	$-0.066T + 44.4$	−0.48	$-0.0015T + 1.4$	−0.086

2006). All the test pieces were heat-treated in advance so that a thermal record by brazing in the actual manufacturing process might be considered.

2.1. Low-cycle-fatigue test in vacuum

A strain-controlled low-cycle-fatigue test was carried out in a vacuum at temperatures of 473 and 573 K. In general, fatigue life in a vacuum is considered to be longer than that in air, because there is no fatigue damage acceleration by oxidation in a vacuum. We defined the fatigue life as the number of cycles at which the peak tensile stress during each cycle dropped by 25% from its initial value (JIS Z2279, 1992). At this number of cycles, around 2 mm-long cracks were typically observed.

We also investigated the effect of the strain waveform on the low-cycle-fatigue life. The real components are subjected to a so-called 'out-of-phase' heat cycle, namely, under compressive stress at high temperature and tensile stress at low temperature. Therefore, the fast–slow test (pc-wave), which is equivalent to the 'out-of-phase' heat cycle, was performed for comparison with the conventional fast–fast test (pp-wave). Fig. 1 shows the effect of the strain waveform on the low-cycle-fatigue life. Although a small difference between the two tests was observed at 573 K, the relationship between the total strain range and the fatigue life in the pc-wave test was in good agreement with that in the pp-wave test. Therefore, we have concluded that the effect of the strain waveform could be neglected at the tested temperatures and the results for both the pc-wave and pp-wave tests could be consolidated.

2.2. $\Delta\varepsilon_t$–N_f diagram of GlidCop

All the data were processed on the basis of the Manson–Coffin equation. The total strain range ($\Delta\varepsilon_t$) is the sum of the plastic strain range ($\Delta\varepsilon_p$) and the elastic strain range ($\Delta\varepsilon_e$), which can be described by approximate equations using the Manson–Coffin's rule and the Basquin's rule, respectively,

$$\Delta\varepsilon_t = \Delta\varepsilon_p + \Delta\varepsilon_e = AN_f^{-\alpha} + BN_f^{-\beta}, \qquad (1)$$

where A, B, α and β are the material properties and N_f is the number of cycles to failure. We attempted to formulate a $\Delta\varepsilon_t$–N_f diagram that can predict the fatigue life at any temperature by using not only the data in a vacuum but also that in air (Takahashi *et al.*, 2006), provided that the multipliers α and β do not depend on the temperature but on the environment. This implies that the temperature- and air-dependent property is only represented by the coefficients A and B. The material properties A, B, α and β are shown in Table 1. Fig. 2 shows the relationship between $\Delta\varepsilon_t$ and N_f derived from the formula (solid lines for air and dashed lines for vacuum), including the experimental results (markers). The observed cycles are in good agreement with the formulated ones. Predictably, it was confirmed that the fatigue life in a vacuum is longer than that in air. For example, when $\Delta\varepsilon_t = 1\%$, the ratios at 473 and 573 K are 2.5 and 2, respectively. In particular, the difference has a tendency to increase on the lower-strain-range region.

3. Fatigue fracture experiment

3.1. Test piece configuration

The test piece was designed such that it fractured in the low-cycle-fatigue region, provided that the maximum temperatures of the absorbing body and the cooling channel are less than 973 K and the boiling point, respectively. Fig. 3 shows the quarter model of the test piece assembly. The model consists of an absorbing body made of GlidCop and a fitting cover and a cooling holder made of stainless steel, all of which are fastened by 12 bolts. The outer diameter of the central absorbing region is 10 mm with a thickness of 2 mm. The important feature of this assembly is its tapered configuration, which is designed with the intention of concentrating the strain in the central area locally. The other feature is that the

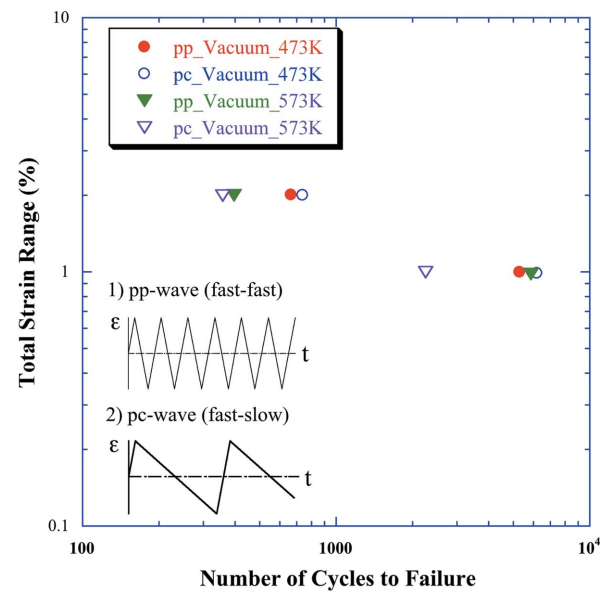

Figure 1
Results of low-cycle-fatigue test in a vacuum. The effect of strain waveform on low-cycle-fatigue life is shown.

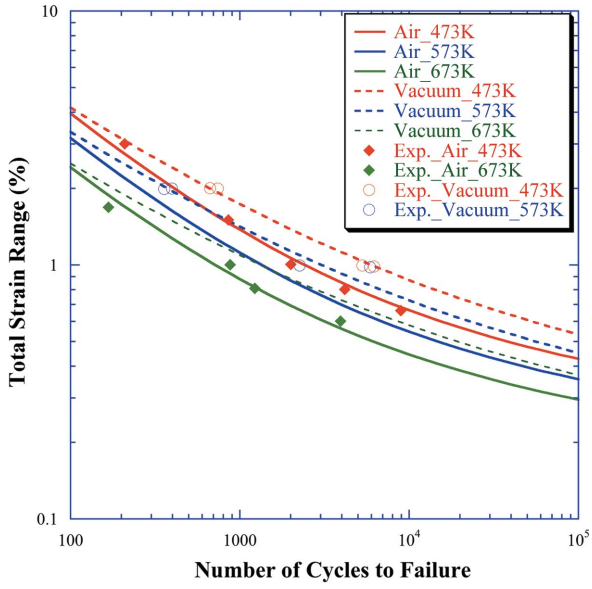

Figure 2
Relationship between $\Delta\varepsilon_t$ and N_f derived from the formula (solid lines for air and dashed lines for vacuum), including the experimental results (markers).

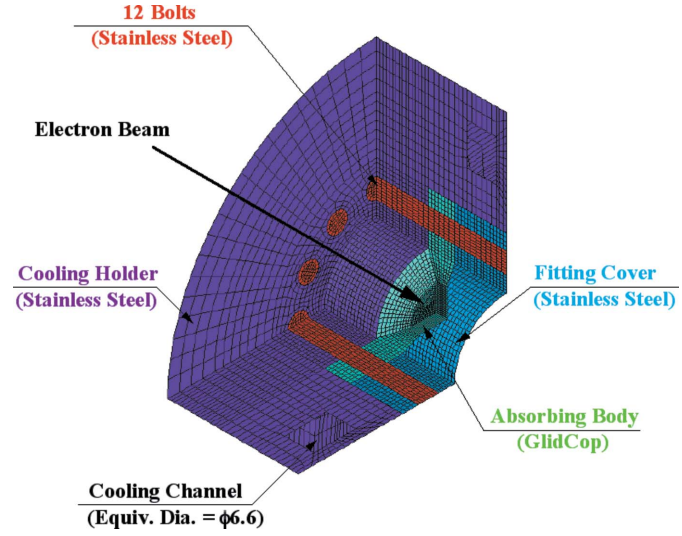

Figure 3
Quarter model of the test piece for the fatigue fracture experiment.

restraining force around the periphery of the GlidCop body is closely maintained by using the axial tension provided by the tightening bolts.

3.2. Experimental set-up

An electron beam gun system was selected as the heat source so that we could confirm the process of fracture at any time. Fig. 4 shows a schematic drawing of the experimental apparatus. It mainly comprises an electron beam gun, a beam stopper, a sample chamber, beam choppers and a Faraday cup. The electron beam, accelerated up to 30 keV, is directed onto the absorbing body after passing through a fixed mask made of tungsten with an aperture size of 8 mm. The beam stopper, which is driven by a pneumatic actuator, works to fully intercept the electron beam, so that the cyclic heat load is generated. One cycle period comprises a 7 min thermal loading condition and 5 min unloading condition. We tested three cases in which the current of the electron beam was adjusted so that it corresponded to 550, 600 and 650 W. The real absorbed power was regarded as the calculated value based on the flow rate and the temperature difference between the inlet and the outlet of the cooling water. It is usually equivalent to about 65% of the computed value based on the accelerating voltage and the output current of the electron beam gun system. The thermocouples for the cooling water were of the T-type with a sheath diameter of 1.0 mm. By using a constant-temperature bath, we confirmed that the relative temperature difference between them was within approximately 0.01 K. The reference temperature was monitored using a K-type thermocouple that was buried into the fitting cover to avoid drilling a hole through the GlidCop body.

3.3. Experimental results

We took out the test piece from the sample chamber after about every 30 cycles, and observed its surface using a digital microscope (VHX-100F manufactured by KEYENCE). Once a crack was detected, a field emission scanning electron microscope (FE-SEM; Quanta200FEG manufactured by FEI Company) was also employed for observation. Figs. 5(*a*), 5(*b*) and 5(*c*) show the 20 magnified FE-SEM photographs of the area around the center of the test piece for an absorbed power of 650 W and 150, 230 and 260 cycles, respectively. Fig. 6 shows

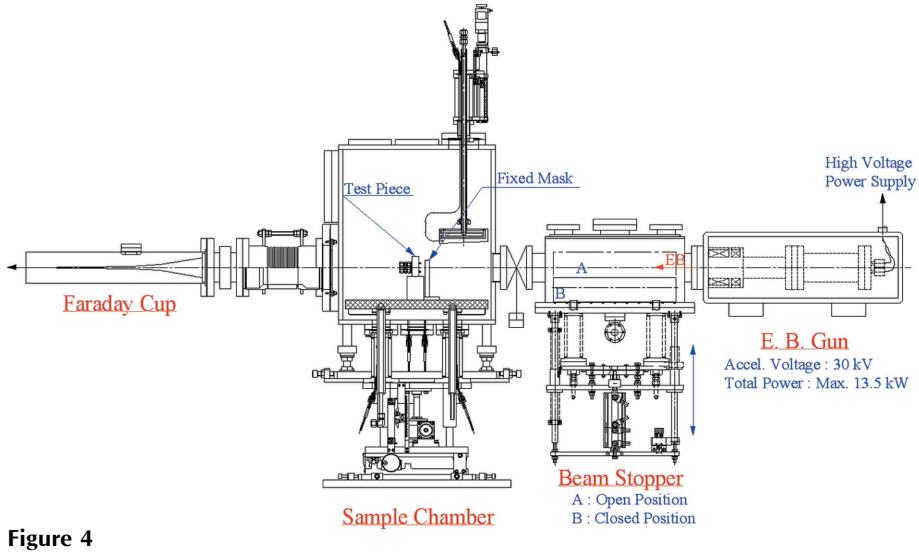

Figure 4
Schematic drawing of the experimental set-up for the electron beam irradiation system.

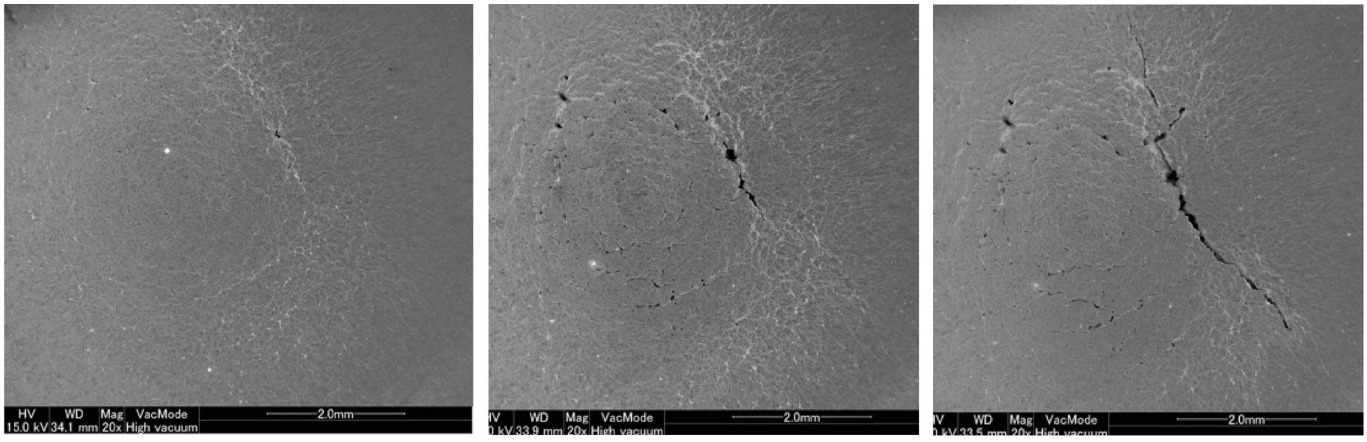

Figure 5
Twenty magnified FE-SEM photographs of the area around the center of the test piece for an absorbed power of 650 W. (*a*) After 150 cycles, (*b*) after 230 cycles, (*c*) after 260 cycles.

the relationship between the crack length and the number of cycles for all cases. Although we cannot state immediately that crack initiation is equivalent to component fracture, the appearance of a crack should be treated as a phenomenon that signals the beginning of fracture after crack propagation. Therefore, in accordance with the results of the low-cycle-fatigue test, the observed fracture life was considered as the number of cycles at which the maximum crack length reaches 2 mm.

4. Elastic-plastic analysis

We conducted an elastic-plastic analysis employing the finite-element analysis program *ANSYS* (http://www.ansys.com).

4.1. Preparation

Beam profiles in both horizontal and vertical directions were independently measured by the beam choppers and the Faraday cup, and fitted by a Gaussian distribution. The power density on each element was calculated depending on the beam profile at the center of the element surface using the following equation,

$$\mathrm{PD}(x, y) = \mathrm{TP} \times \frac{1}{2\pi\sigma_x\sigma_y} \exp\left(-\frac{x^2}{2\sigma_x^2} - \frac{y^2}{2\sigma_y^2}\right), \qquad (2)$$

where PD(x,y) is the power density at the center of the element surface (x,y), TP is the real absorbed power, and σ_x and σ_y are the standard deviations along the horizontal and the vertical directions, respectively. The power density is given as the surface load on an element. In the case of the total power of 650 W, the peak power density on the absorbing body reaches about 56 W mm^{-2}, as shown in Fig. 7. Based on the Dittus–Boelter's equation, the heat transfer coefficient of the cooling channel was 6200 W m^{-2} K^{-1} with a flow rate of 3 L min^{-1} and the equivalent diameter of the rectangular cooling channel. The bulk temperature of the cooling water was set to 305 K. We defined some contact elements on the surface of contact between the GlidCop and the stainless steel,

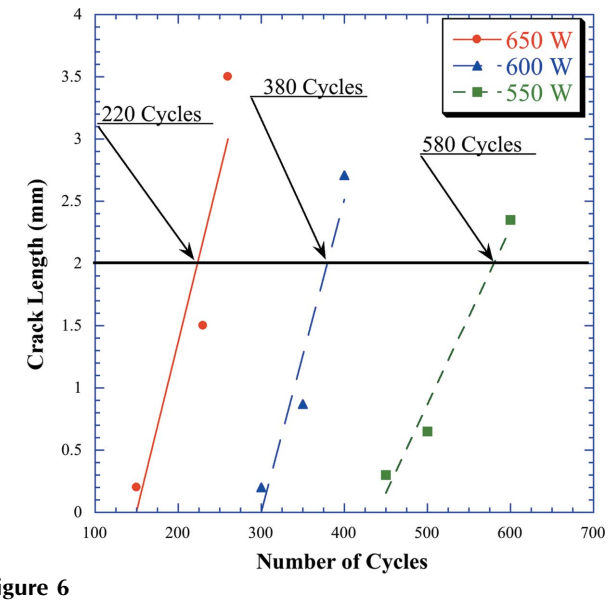

Figure 6
Relationship between the crack length and the number of cycles for absorbed power of 550 W and 650 W.

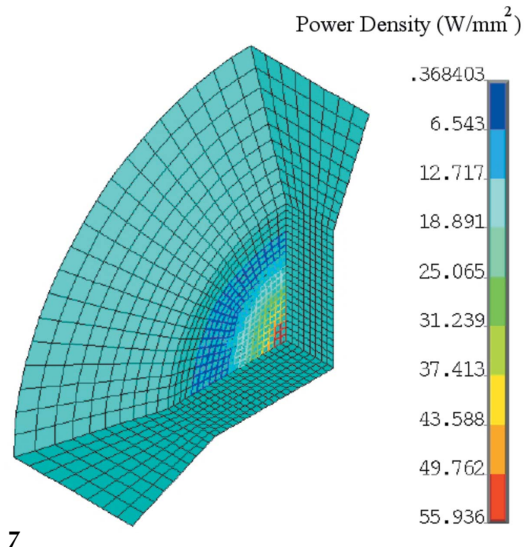

Figure 7
Spatial distribution of the heat flux in the model. The heat flux is given as the surface load on each element.

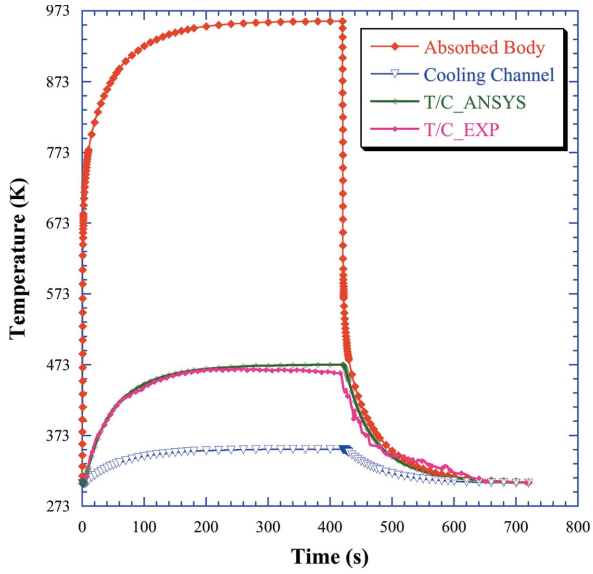

Figure 8
Transient nodal solutions of the maximum temperatures on the absorbing body and the cooling surface when the absorbed power is 650 W. The measurements of the reference temperature (T/C_EXP) and the nodal solutions (T/C_ANSYS) at the location of the K-type thermocouple are also shown.

wherein an adequate thermal contact conductance of about 5000 W m^{-2} K^{-1} was set.

Fig. 8 shows the transient nodal solutions of the maximum temperatures on the absorbing body and the cooling surface when the absorbed power is 650 W. The measurements of the reference temperature and the nodal solutions at the location of the K-type thermocouple are also shown in Fig. 8. Because the measurements and the calculations are in fair agreement, we confirmed that the boundary conditions employed for the thermal analysis are adequate.

As shown in Fig. 9, the temperature-dependent true stress and true strain diagrams in the plastic strain region were

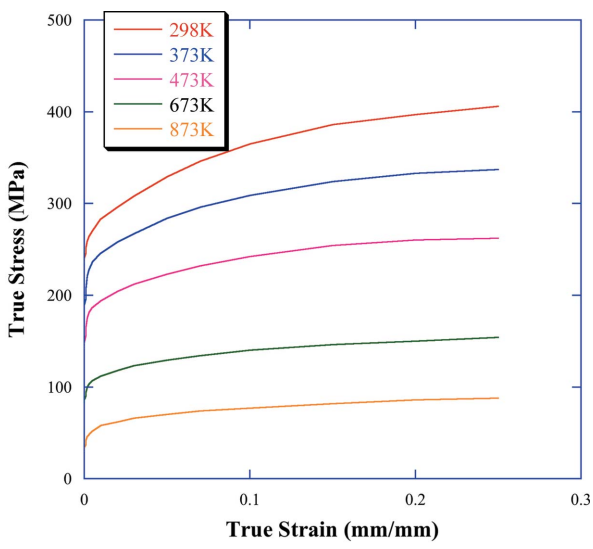

Figure 9
Temperature-dependent stress–strain diagrams in the plastic strain region of the GlidCop body.

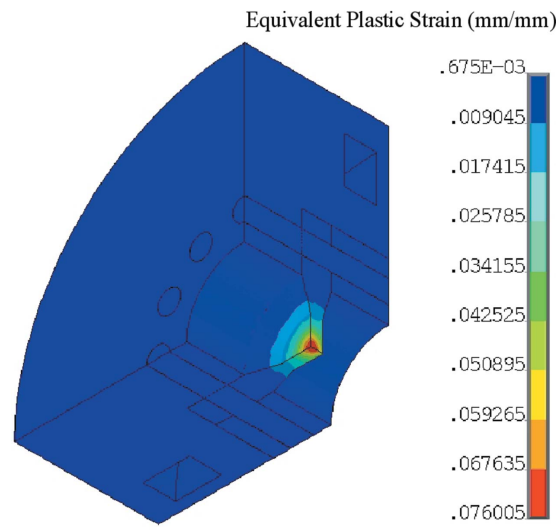

Figure 10
Contour plot of the equivalent plastic strain just before the eighth irradiation was stopped.

prepared based on the tensile test results (Takahashi *et al.*, 2006). In the *ANSYS* solution they are approximated by multiple straight lines, namely by using the multi-linear option. Because a cyclic thermal loading with compressive and tensile stresses was applied in this case, the kinematic hardening rule, which includes the Bauschinger effect, was selected.

4.2. Analysis results

The elastic-plastic analysis without considering the effect of creep was performed by applying a cyclic heat load of 650 W eight times. Fig. 10 shows a contour plot of the equivalent plastic strain just before the eighth irradiation was stopped. Since the maximum value of the equivalent plastic strain appears at the center of the GlidCop body, the hysteresis loop of the total strain and the equivalent stress is drawn by the elemental solutions of the central element, as shown in Fig. 11. After eight heat cycles, the total strain range converges to about 2.64% and is composed of 2.34% plastic strain range and 0.30% elastic strain range. The symbols S and F in Fig. 11 indicate the start and finish points of the second heat loading, respectively. In this case the repeated occurrence of a tensile stress at low temperature and a compressive stress at high temperature was observed. The analysis results, including the boundary conditions, for several heat-load cases are summarized in Table 2. Although we did not perform the fatigue tests, the results for the two cases of lower heat loads (400 W and 500 W) are also listed in Table 2 for reference.

4.3. Influence of creep

We conducted creep tests for GlidCop at temperatures of 373, 473, 673 and 873 using the same heat-treated test pieces as those used in the low-cycle-fatigue test in order to develop a creep constitutive equation for *ANSYS*. We selected the Norton model, which only considers secondary creep, from 13

Table 2
Analysis results, including the boundary conditions, for several heat-load cases.

The mean temperature, with a high temperature corresponding to the maximum temperature and a low temperature of 305 K, is used for the estimation of A and B in equation (1). The estimated fatigue lives according to equation (1) are also listed.

		Body temperature (K)		Strain range (%)			
Total power (W)	Maximum power density (W mm^{-2})	Maximum	Mean	Plastic	Elastic	Total	Estimated life (number of cycles)
400	34.4	702.7	504	0.68	0.34	1.02	4585
500	43.0	804.4	555	1.27	0.32	1.59	807
550	47.3	855.7	580	1.61	0.30	1.91	405
600	51.6	907.2	606	1.96	0.28	2.24	221
650	56.0	958.9	632	2.34	0.30	2.64	121

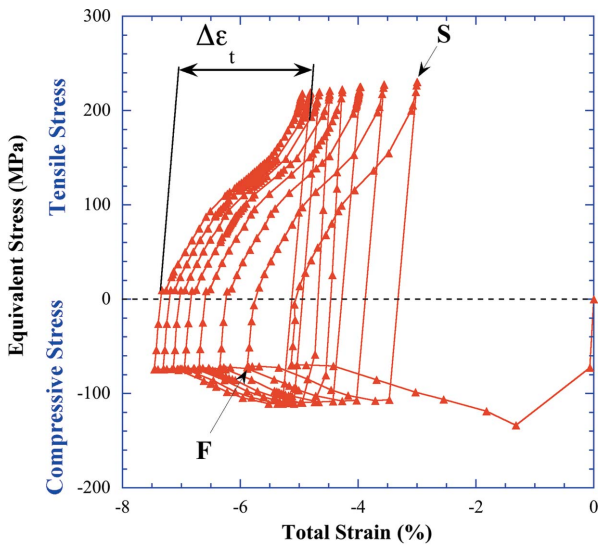

Figure 11
Hysteresis loop of the total strain and the equivalent stress based on the elastic-plastic analysis with the multi-linear kinematic hardening option. The symbols S and F indicate the start and finish points of the second heat loading, respectively.

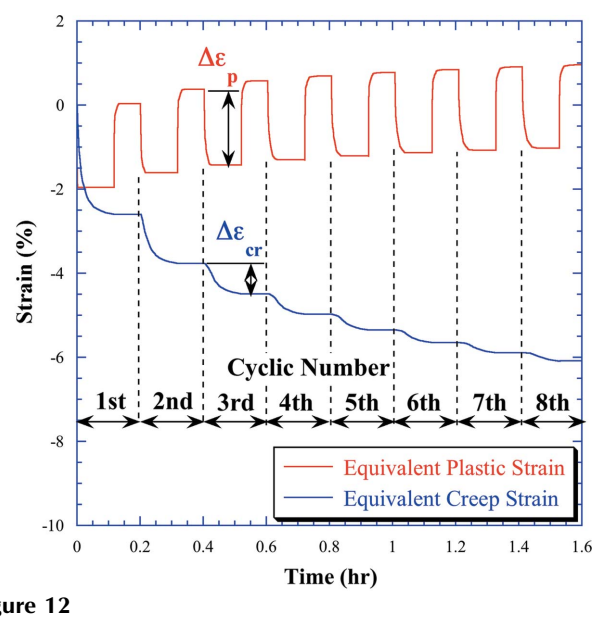

Figure 12
Time history of the equivalent plastic strain and the equivalent creep strain for the elastic-plastic plus creep analysis with the Norton model.

creep models that *ANSYS* provides. This is the reason why the primary creep did not influence the creep strain, except in the first cycle of cyclic heat loading.

Fig. 12 shows the time history of the equivalent plastic strain and the equivalent creep strain for the elastic-plastic plus creep analysis with the Norton model, separately. Although the creep strain range at the first cycle of 2.6% is larger than the plastic strain range of 2.0%, it gradually decreases and eventually reaches about 0.2% at the eighth cycle. On the other hand, because the plastic strain range is almost constant at about 1.9% regardless of the cycle number, it can be said that the plastic strain dominates the entire fatigue behavior. Consequently, in this case, we decided that it is not necessary to consider the effect of creep in fatigue life prediction.

4.4. Discussion

After obtaining the above-mentioned results concerning the effect of creep, we calculated the fatigue life according to equation (1) based on the total strain range of $\Delta\varepsilon_t$ that was determined by the elastic-plastic analysis with the multi-linear kinematic hardening option. The material properties A, B, α and β in equation (1) were estimated by the mean temperature, with a high temperature corresponding to the maximum temperature and a low temperature of 305 K. The calculated fatigue lives are shown in Table 2. Fig. 13 shows the relationship between the observed life and the predicted fatigue life. The two dashed lines indicate a factor of two on life. The

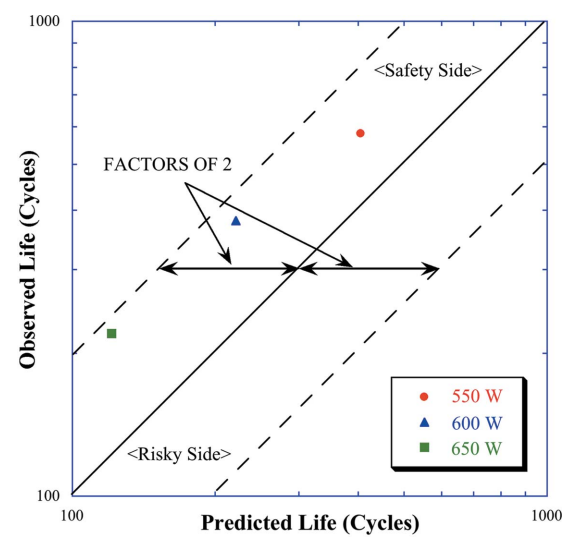

Figure 13
Relationship between observed and predicted fatigue life. The two dashed lines indicate a factor of two on life.

observed life was within a factor of two when compared with the predicted life, yet located on the safer side.

5. Conclusions

From the results of low-fatigue-cycle tests on a study GlidCop body in both air and a vacuum, the environment-dependent relationship between the total strain range and the fatigue life at any temperature has been presented; this relationship is based on the Manson–Coffin equation. We applied a cyclic heat load to a specially designed test piece by using an electron beam irradiation system, and continuously observed the fracture behavior, namely crack initiation and propagation, by FE-SEM, to determine the observed life. In addition, the fatigue life was predicted by the hysteresis loop of the elastic-plastic analysis with the multi-linear kinematic hardening option using *ANSYS*. Furthermore, based on the results of creep tests, we confirmed that the creep phenomenon would not influence the fatigue life in this case through the elastic-plastic plus creep analysis. Thus, we could confirm that the observed life was within a factor of two when compared with the predicted life.

Based on the results of these tests, the thermal limitation of currently existing high-heat-load components of SPring-8 front ends made of GlidCop can be detected, and this is the subject of our future study.

The authors would like to thank Drs Yokomaku and Nakayama of KOBELCO Research Institute for valuable discussions and comments.

References

Hara, T., Tanaka, T., Kitamura, H., Bizen, T., Marechal, X., Seike, T., Kohda, T. & Matsuura, Y. (2004). *Phys. Rev. ST-AB*, **7**, 050702.

JIS Z2279 (1992). Japanese Industrial Standard, *Method of high-temperature low-cycle fatigue testing for metallic materials.*

Mochizuki, T., Takahashi, S. & Kitamura, H. (2003). *Proceedings of the Eighth International Conference on Synchrotron Radiation Equipment and Instrumentation*, San Francisco, CA, USA, pp. 474–477. Melville: American Institute of Physics.

Oura, M., Sakurai, Y. & Kitamura, H. (1998). *J. Synchrotron Rad.* **5**, 606–608.

Ravindranath, V., Sharma, S., Rusthoven, B., Gosz, M., Zhang, L. & Biasci, J. (2006). *Proceedings of the International Workshop on Mechanical Engineering Design of Synchrotron Radiation Equipment and Instrumentation 2006*, Himeji, Hyogo, Japan.

Takahashi, S., Sano, M., Mochizuki, T., Watanabe, A. & Kitamura, H. (2006). *Proceedings of the International Workshop on Mechanical Engineering Design of Synchrotron Radiation Equipment and Instrumentation 2006*, Himeji, Hyogo, Japan.